Rare-earth element and stable isotope signatures of kaolin from a Pliocene lateritic weathering profile at mid-latitude region (Andalusia, Spain): Implications for paleoweathering and paleoclimatic reconstructions

Juan Carlos Fernández-Caliani
Department of Earth Sciences, University of Huelva, Campus de El Carmen s/n, 21071 Huelva, Spain

Abstract

This study reports the impact of weathering on behavior of rare earth elements (REE) in a coastal lateritic profile developed on Pliocene sediments at mid-latitude location (~37º N), in the Guadalquivir Basin (Spain). It also explores the stable isotope signature of kaolinite providing constraints on paleotemperature and isotopic composition of the ancient meteoric water. The paleoweathering profile (~20 m thick) comprises a white sandy clayey saprolite overlain by a red-mottled clay zone, which in turn is capped by a pisolitic ferricrete. The kaolinitic regolith was practically reduced to a mixture of kaolinite and quartz by intense chemical weathering under warm and seasonally humid climate.

The kaolinized material is markedly depleted in total REE (mean value of 77.30 mg kg^{-1} in the white saprolite and 72.70 mg kg^{-1} in the mottled zone) relative to the parent rock (168.96 mg kg^{-1}). Development of acidic and oxidizing conditions promoted a suitable soil environment for REE release and leaching with percolating rainwater, leading to an apparent loss of REE from the profile (up to 87%). The parent rock-normalized REE patterns display concave-upward shapes tracing a remarkable depletion in middle REE (MREE), with no significant anomalies. The REE concentrations normalized against the NASC showed consistently similar fractionation patterns. The MREE-depleted signature (La_N/Sm_N ratio up to 3.32 and Gd_N/Lu_N ratio as low as 0.45) probably arises from reductive dissolution of iron oxyhydroxide phases due to seasonal water saturation, as indicated from redoximorphic features.

The <2 mm kaolinite separates showed $d^{18}O$ values ranging from 17.3‰ to 20.0‰, and dD values between -71‰ and -60‰. The $\delta^{18}O$ and δD mean values indicated a crystallization temperature of about 24ºC, which is higher than the local present-day annual mean air temperature (~18ºC). For the calculated temperature, the oxygen isotope fractionation factor between kaolinite and water (a_{k-w}= 1.0248) implies that kaolinite formed in equilibrium with meteoric waters ($d^{18}O$= -5.4‰ and dD= -33‰) that closely reflect the regional meteoric precipitation.

The lateritic weathering profiles evolved during the mid-Pliocene warm period in the southwestern Iberian margin could be useful for predicting potential future environmental effects of increased atmospheric CO_2 on the Earth´s critical zone.

Key words: kaolinite; laterization; paleosol; climate change; Guadalquivir Basin

1. Introduction

Paleoweathering profiles are a major record of Earth´s surficial conditions because they represent fundamental events (climatic, tectonic, etc.) that assist in stratigraphical correlation and give precise information on past environmental conditions (Thiry et al., 1999). Within the context of the lateritic environment, deeply kaolinized profiles may have important implications for paleoclimatic and paleoweathering reconstructions. Kaolinization is a prominent weathering process in the intertropical rainy zone that usually leads to the formation of large kaolin deposits on extensive lateritic mantles (e.g. Ambrosi and Nahon, 1986; Tardy and Roquin, 1992; Schaefer et al., 2008). In fact, kaolinite is an abundant clay mineral in paleosol profiles that formed in paleotropical sites (e.g. Sheldon and Tabor, 2009).

However, the stable isotope composition of kaolinite reveals that much of the kaolinitic regoliths formed under relatively cold conditions, suggesting that, contrary to classical interpretations, laterization and deep weathering phenomena are not solely the result of weathering in tropical or subtropical climates (Bird and Chivas, 1989). It has been also suggested that development of kaolinitic profiles at extra-tropical latitudes may be the result of a greenhouse warming induced by increased atmospheric CO_2 levels (e.g. Dowsett et al., 1992; Barron et al., 1993; Thiry, 2000; Krause et al., 2010). Thus, the areal distribution of kaolin means in effect the presence of a “cool” and “warm” kaolinization, one of moderate intensity in the humid mid-latitude climatic zone, and the other one much bigger in size and more variable in the mineral assemblage, typical of the humid tropical climate zones (Dill, 2016).

Ancient kaolinitic weathering surfaces currently exposed to non-tropical alteration conditions have been recognized in the southwestern corner of the Iberian Peninsula, both in Portugal (Marques et al., 1980-81; Abreu, 1990) and Spain (Rodríguez-Vidal et al., 1985; Núñez and Recio, 2007; Díaz del Olmo et al., 2010; Fernández-Caliani and Cantano, 2010). The Bonares profile is a relict paleosol formed on the kaolinized past landscape that has fortunately been preserved in the geological record of the Guadalquivir Basin (Spain). The kaolinization process was described by Fernández-Caliani and Cantano (2010) in terms of major and trace element distributions, excluding rare earth elements (REE), with the preliminary results being consistent with a lateritic weathering profile evolved under humid subtropical conditions during late Neogene time. The present paper revisits the issue by providing new insights from REE geochemistry and stable isotope data.

Research on geochemistry of REE in paleosol studies has gained considerable prominence over the last decade. This increasing interest is based on the fact that the REE patterns can be used as promising tracers of past water-rock interaction and soil formation processes (Minarik et al., 1998; Taunton et al., 2000; Laveuf et al., 2008; Vermeire et al., 2016), and they can aid in monitoring the impact of weathering on REE mobilization and fractionation (Öhlander et al., 1996; Laveuf and Cornu, 2009; Ma et al., 2011; Yusoff et al., 2013; Jin et al., 2017). Isotope geochemistry is another major contributor to paleoweathering studies. Stable isotope ratios of hydroxylated soil minerals can serve as a proxy for the temperature of formation and the isotopic composition of the water from which they crystallized, which in turn provide information about past surface air temperatures (Lawrence and Taylor, 1972; Delgado and Reyes, 1996; Tabor and Montañez, 2005; Clauer et al., 2015; Hall et al., 2015).

Also, stable isotope analysis is usually applied in paleosol studies to reconstruct environmental and/or climatic conditions that prevailed at the time of soil formation (Savin and Hsieh, 1998; Girard et al., 2000; Yapp, 2000; Feng and Yapp, 2009; Sheldon and Tabor, 2009; Rosenau and Tabor, 2013).

The present study was specifically aimed at determining: (1) the effects of weathering on distribution, mobility and fractionation of REE in the lateritic profile of Bonares with a view to tracing the geochemical behavior of REE during the formation of the kaolin-enriched paleosol; and (2) the hydrogen and oxygen stable isotope ratios of kaolinite to constrain the isotopic composition of the local meteoric water and temperature of the ancient weathering system.

2. Geological setting and description of the profile

The Bonares lateritic profile is located at the northwestern margin of the Guadalquivir Basin, an ENE-WSW elongated basin developed during the Neogene and Quaternary between the external units of the Betic Cordillera and the Iberian Massif, in southwestern Spain (Fig. 1). This foreland basin occupies a strategic position for studying the interplay between lithospheric and surface processes, and may help in the understanding the tectonic and climatic factors controlling the connection between the Mediterranean Sea and the Atlantic Ocean (Larrasoaña et al., 2013).

The paleoweathering profile developed over the locally named Bonares Sands Formation, which constitutes the last Neogene depositional sequence at the west end of the Guadalquivir Basin (Sierro et al., 1996). The formation is composed mainly of highly permeable arkosic sands, with gravel lenses and layers, representative of tidally-influenced foreshore sedimentation (Mayoral and Pendón, 1986-87), although the upper formation probably was part of a braided fluvial system feeding deltaic and shallow-marine environments. An erosional surface or erosive unconformity separates these siliciclastic deposits from the underlying Huelva Sands Formation, which is characterized by fine-grained sands and sandy silts with large accumulations of mollusk shells of early Pliocene age (Civis et al., 1987). The Neogene formations appear unconformably overlaid by coarse-grained sands and gravels deposits conditioned by the Quaternary evolution of the fluvial network of the Tinto river, a naturally acidic system fed by subsurface bioxidation of sulfide orebodies (Gómez-Ortiz et al., 2014) and, additionally, severely affected by acid mine drainage (Galán et al., 2003).

The altitude of the area ranges between 120 and 140 m above sea level and the present climate is oceanic Mediterranean, with mean annual precipitation of about 525 mm, and mean annual temperature around 18.2ºC. The relative humidity remains moderately high (up to 80%) due to the proximity to the Atlantic Ocean.

The Bonares profile (Fig. 2) can be subdivided from bottom to top into four zones, with an overall exposed thickness of about 20 m at this location (Fernández-Caliani and Cantano, 2010):

- Zone I (parent material): it consists mainly of yellowish orange (10YR 7/6, Munsell color chart), fine to medium-grained sands displaying parallel lamination and gentle cross-bedding dipping in opposite directions.

• Zone II (10-12 m thick): a white (10YR 8/1) sandy clayey saprolite in which sedimentary structures of the parent rocks are still well preserved and recognized (Fig. 2a,b). This saprolitic horizon is referred to as lithomarge by Rodríguez-Vidal et al. (1985).

• Zone III (3-4 m thick): a mottled clay horizon showing a distinct contrast between brown-red colored (10R 5/8) and bleached (7.5YR 8/3) domains (redoximorphic features). In this horizon the original structure of the parent rock was completely obliterated (Fig. 2c). The mottled zone can be regarded as an old plinthic horizon similar to those found in lateritic profiles.

• Zone IV (0-1 m thick): the profile is capped by a purple-reddish (10R 3/2) duricrust palesosurface with a pisolitic structure (Fig. 2c), partially dismantled by erosive processes. In places, a soft clay layer occurs at the base of the duricrust. The remnants of the pisolitic duricrust can be seen only on highest parts of the present-day landscape.

3. Material and methods

The outcrops of the lateritic paleosol sampled for this study are located around Bonares, approximately 30 km east of Huelva (SW Spain), on the left bank of the Tinto river (Fig. 1). Seventeen kaolin samples were collected at different depths of the lateritic paleosol from three vertical cross-sections located at the following geographic coordinates (referred to UTM zone 29N): section 1 (37º18´42´´N-6º40´26´´W), section 2 (37º19´35´´N-6º40´21´´W) and section 3 (37º19´55´´N-6º38´52´´W). Section 1 shows the upper-middle part of the lateritic paleosol, section 2 exposes the saprolite horizon and the bedrock, while section 3 is representative of the entire weathering profile. The sample PTB-1 was used as a proxy for the average composition of the parent rock from which the paleosol developed.

Particle-size distribution was measured by laser diffraction with a Mastersizer 2000 (Malvern Instruments). Mineralogical analysis was conducted by X-ray powder diffraction (XRD) on a Bruker-AXS D8-Advance diffractometer, using monochromatic CuKα radiation at 40 kV and 30 mA. Whole-rock random powders were scanned over a range of 3 to 65° 2Θ, using a step size of 0.02º 2Θ and 0.6 s count time per step, after gentle grinding and homogenization. Sample aliquots were disaggregated by ultrasonic agitation in deionized water and the <2 μm size fraction was separated by wet sieving and centrifugation after dispersion. The clay separates were transferred to glass slides as oriented aggregates, air-dried, and then scanned from 1 to 30° 2θ using a step size of 0.02º 2θ and a counting time of 1.2 s per step. The oriented clay fractions were solvated with ethylene glycol and dimethyl sulfoxide, and subjected to thermal treatment at 550°C for 2 h, in order to identify clay minerals precisely. The XRD patterns were recorded by means of the software DIFFRACplus (Bruker-AXS) linked with a reference database, and estimates of mineral abundance were made by using mineral intensity factors (Moore and Reynolds, 1997).

A few kaolin samples representative of each horizon were selected for high-resolution observation by scanning electron microscopy (SEM) on a FEI Quanta 200 instrument, operated at 20 kV accelerating voltage, equipped with an energy dispersive X-ray (EDS) detector. The main purpose was to recognize REE-bearing minerals and other accessory phases by combining secondary electron (SE) and back-scattered electron (BSE) imaging with EDS analysis. The quantitative EDS analyses were performed using a standardless method.

The REE concentrations in whole-rock samples were analyzed, after grinding to analytical fineness, by inductively coupled plasma-mass spectrometry (ICP-MS) on a Perkin Elmer Optima 3000 after a lithium metaborate/tetraborate fusion technique that ensures the entire sample dissolution. Quality control of the analytical procedure included the use of a method reagent blank, several certified reference materials (BIR-1, DNC-1, GXR-1, GXR-2, LKSD-3, MAG-1, MICA-Fe, WMG-1, and W-2a), and replicates by the laboratory to check accuracy and precision of the data. The relative deviations of the standard analyses to the reference values were typically below 10%. In order to eliminate the Oddo-Harkins effect and to characterize the REE fractionation patterns, the concentrations of individual REE were normalized relative to the parent rock (internal reference) and the North American Shale Composite (NASC), which represents REE abundances in the upper continental crust (Gromet et al., 1984). Normalized values and ratios of normalized values are denoted with the subscript N.

A selection of clay separate samples from the highly kaolinitic saprolite was chosen for isotopic analysis. The clay separates consisted of more than 95% kaolinite with minor impurities of quartz, as confirmed by XRD and SEM-EDS analyses. Isotope stable measurements were done by Activation Laboratories (Ancaster, Ontario, Canada), which is accredited against ISO/IEC 17025 Quality System, using a Thermo-Finnigan DeltaPlus XP continuous-flow isotope-ratio mass spectrometer.

For oxygen isotope analysis, the samples were reacted with BrF_5 at about 650°C in nickel bombs following the procedures described in Clayton and Mayeda (1963). The fluorination reaction converts O in the minerals to O_2 gas, which is subsequently converted to CO_2 gas using a hot C rod. For hydrogen isotope analysis, the samples were wrapped in molybdenum foil and placed in a platinum crucible, which was then suspended inside a quartz extraction vessel. The vessel and its contents were outgassed in a vacuum at 120°C for 4 h to remove surface-adsorbed water. The samples were then inductively heated at 1400°C for up to 20 min and the gases were collected in a trap held at -196°C. Nearly all of the hydrogen was released in the form of water, but miniscule quantities of hydrocarbons or molecular hydrogen released or produced during this treatment were oxidized over CuO at 550°C to form H_2O and CO_2 which were also collected in the trap. The accumulated water representing the total amount of hydrogen in the samples was separated from the other gases by differential freezing techniques. The water was reacted with uranium at 900°C to produce H_2 and collected on charcoal at -196°C. The volume of the H_2 was measured manometrically.

Oxygen and hydrogen isotope compositions are reported with the usual delta (δ) notation as per mil deviations from the Vienna Standard Mean Ocean Water (V-SMOW), where: $\delta X = (R_{sample} / R_{V\text{-}SMOW} - 1) \times 1000$.

For $X = {}^{18}O$, $R = {}^{18}O/{}^{16}O$, whereas for X= D, R= D/H.

Overall analytical precision of the isotopic measurements is estimated at ±0.1‰ for $\delta^{18}O$ values and ±3‰ for δD values at one sigma.

4. Results and discussion

4.1 Mineralogical and geochemical trends

The results of the mineralogical analysis (Fig. 3) showed that the parent rock is composed mainly of quartz, alkali feldspars and clay minerals (mica, smectite and kaolinite in this order of abundance) together with heavy accessory phases, notably ilmenite, rutile, monazite and zircon.

Practically, the regolith was reduced to a simple mixture of kaolinite and quartz by intense chemical weathering of the underlying bedrock. The saprolite zone consists of unconsolidated kaolinitic sand with a bimodal particle-size distribution (Fig. 4), containing quartz and kaolinite in varying proportions, and minor resistant heavy minerals and opaline material. Although strongly altered, alkaline feldspar is still present as skeletal crystals in the kaolinized material. Kaolinite comprises almost the entire clay mineral assemblage. It typically occurs as tiny partly pseudo-hexagonal plates, although booklets forming vermiform aggregates were also observed by SEM. Hinckley crystallinity index values of kaolinite declined upwards in the profile from 1.7 to 1.1, indicating a decreasing degree of structural order with advancing kaolinization.

The overlying mottled zone is characterized by the occurrence of goethite, hematite and poorly-crystallized iron oxyhydroxides which completely mask the white color of the kaolin. The soft layer observed at the top of the mottled zone contains a high proportion of kaolinite, appreciable amounts of goethite, and minor gibbsite and boehmite. Finally, the pisoliths from the ferruginous crust capping the profile are made up of quartz grains embedded in a ferruginous matrix containing goethite, hematite, maghemite and scarce kaolinite.

Monazite was the only significant REE-rich mineral found as an accessory phase in the kaolin. It was observed exclusively in the incipiently kaolinized parent rock, as evidenced by SEM-EDS examination (Fig. 5). The EDS microanalysis revealed that isolated, subhedral crystals of monazite (up to 100 μm in length) from the sample BO-0 contain appreciable amounts of Ce, La, Nd, and to a lesser extent Pr, Sm, Gd, Th and U.

Kaolinite was formed by incongruent dissolution of primary silicates, mainly alkali feldspars and micas, through the following acid hydrolytic reactions:

$$2NaAlSi_3O_{8\ (\text{Na-feldspar})} + 9H_2O + 2H^+ \rightarrow Al_2Si_2O_5(OH)_{4\ (\text{kaolinite})} + 4H_4SiO_4 + 2Na^+$$

$$2KAlSi_3O_{8\ (\text{K-feldspar})} + 9H_2O + 2H^+ \rightarrow Al_2Si_2O_5(OH)_{4\ (\text{kaolinite})} + 4H_4SiO_4 + 2K^+$$

$$2KAl_3Si_3O_{10}(OH)_{2\ (\text{muscovite})} + 3H_2O + 2H^+ \rightarrow 3Al_2Si_2O_5(OH)_{4\ (\text{kaolinite})} + 2K^+$$

Accordingly, the weathering process is geochemically characterized by striking losses of Na, K, Ca, Mg and large-ion lithophile elements (Rb, Sr, Cs, Ba, and U), whereas Al, Si and Fe remained relatively immobile and residually concentrated in the profile along with a variety of trace metals including Sc, V, Cr, Nb, Ta, and Th (for further details on these findings see previous work by Fernández-Caliani and Cantano, 2010). Most of soluble basic cations released from the breakdown of silicates were easily leached and lost in solution, as evidenced by the shifting of the chemical index of alteration of Nesbitt and Young (1982), from a value of 77 in the fresh parent material to 97 in the upper (most weathered) part of the profile (Fig. 3).

The alteration process took place in-situ and any reworking of the kaolin can be ruled out. Therefore, the mineralogical and major element signatures recorded in the kaolinitic regolith are consistent with high rates of infiltration and efficient leaching of soluble cations. The purity of the kaolinitic clay and silica sand may be the result of intense weathering in a humid subtropical climate with high rainfall. Similar trends have been reported elsewhere in surface and near-surface environments where there is evidence of formation of kaolinite under acidic, warm and humid conditions in well-drained soils with very low base cation activity in soil solutions (e.g. Dixon and Weed, 1989; Velde and Meunier, 2008; Galán and Ferrell, 2013), such as prevail in tropical and sub-tropical regions today.

4.2 Effects of weathering on REE depletion

Individual REE and total REE concentrations (ΣREE) varied depending on the sampling location in the profile (Table 1). The ΣREE concentrations ranged between a minimum of 32.38 mg kg^{-1} (sample BO-3) up to a maximum of 202.35 mg kg^{-1} in the incipiently weathered material occurring in the basal saprolite zone (sample BO-0). Indeed, the highest concentrations of total REE were recorded in, or proximal, to the unaltered parent rock. Cerium was the most abundant among the REE with 89 mg kg^{-1}, followed by Nd (39.6 mg kg^{-1}) and La (32.6 mg kg^{-1}). These results are in agreement with the occurrence of monazite, the major source of light REE (LREE) present at the base of the paleoweathering profile.

The overall REE abundance in the kaolinitic regolith (mean value of 77.30 mg kg^{-1} in the white kaolinitic sands and 72.70 mg kg^{-1} in the red ones) was found to be noticeably low relative to the bedrock (168.96 mg kg^{-1}), as well as when compared with the average value (146.37 mg kg^{-1}) of the upper continental crust (Taylor and McLennan, 1985). Therefore, the kaolinized material seems to be much more depleted in REE than the parent rock, suggesting high water-rock interaction under acidic weathering conditions (Ma et al., 2011).

Mobilization and redistribution of REE, reflecting the water-rock interaction processes during the paleoweathering event, was investigated by normalizing each REE to Ti, which is assumed to be a lithogenic conservative element (Nesbitt, 1979). The REE and Ti abundances in the parent rock exposed to weathering (sample PTB-1) were used as reference in the mass-balance calculations, assuming that potential error is restricted to local heterogeneities in the protolith. The Ti-normalized distribution patterns (Fig. 6) showed that the REE losses increased progressively upwards reaching up to 87% at the top of the profile, where the intensity of chemical weathering was more intense. In other words, the REE budget in the kaolinized material decreased with increasing degree of weathering, as generally reported in the literature (e.g. Braun et al., 1993; Laveuf and Cornu, 2009; and references therein).

The isocon diagrams provide a graphical method to evaluate which REE are immobile, gained or lost during weathering (Moore, 1996). Losses of REE have been estimated at constant mass relative to line of equal concentration (isocon) that fits well the immobile elements (e.g. Ti, Fe, Al). As shown in Figure 7, all the REE lie below the isocon, indicating that they were lost in the course of kaolinization. The deviation of the data point from the isocon defines the elemental concentration change. Thus, Ce, La, Nd, Sm, Gd and Dy were subjected to the greatest loss compared to their abundances in the parent rock. The other REE fall close to the isocon, and so they were removed from the profile to a lesser extent.

4.3 Mobility and fractionation of REE

It is widely known that mobilization, and finally depletion, of REE in soil is strongly dependent on the acidity of the soil solution (Cao et al., 2001; Marker and Oliveira, 1994; Fernández-Caliani et al., 2009; Welch et al., 2009). Solubility of REE is typically low at near neutral pH but it tends to increase with soil acidity. It is plausible that development of acidic and oxidizing conditions promoted a suitable environment for REE leaching with percolating rainwater after released from primary minerals, resulting in an apparent net loss of REE from the soil profile. The REE were relatively geodisponible despite the well-known resistance of REE-bearing accessory minerals to weathering (e.g. monazite and zircon). Release of relatively immobile elements, such as REE and Zr, is a process frequently reported in laterites, particularly under acid conditions with significant chloride concentrations, as expected in most of the lateritic profiles developed near coastal zones (Colin et al., 1993).

Given that monazite is the main contributor to the LREE budget in the source rock, the fact that kaolin is depleted in ΣREE, prevalently in LREE, suggests that a major part of REE was leached out of the profile after being released from monazite by dissolution through reaction with acidic soil water. Otherwise, the REE should remain immobilized in the residual kaolin, either hosted in resistant crystals of monazite (Galán et al., 2007; Fernández-Caliani et al., 2010); bound to kaolinite by sorption mechanisms

(Aja, 1998; Coppin et al., 2002; Wang and Liu, 2005); or coprecipitated with newly-formed phases (Bau, 1999), thus leading to overall enrichments in REE. Seemingly, secondary phases did not play an important role in the retention of the REE in the paleosol through one or a combination of the two latter mechanisms. Another possibility is that the REE were originally retained in the mottled zone by adsorption onto iron oxyhydroxides, and then remobilized under secondary redox conditions (Laveuf et al., 2012) related to seasonal rising water table, with the leached material lost to the drainage network.

The REE patterns of the kaolin normalized relative to the parent rock (Fig. 8) do not only confirm the depletion in terms of REE concentration level, but also evidence that they were not transferred unmodified from the protolith to the kaolinitic regolith, thereby suggesting fractionation during paleosol development. The parent rock-normalized REE patterns are almost parallel for most individual samples, with no significant anomalies. They do not display a remarkable LREE/HREE fractionation, as indicated by the low La_N/Lu_N ratios (1.74 on average), but rather a striking depletion in middle REE (MREE) in comparison to the other REE. In fact, the highly kaolinized samples exhibit concave-upward morphologies defined by a steady decrease in the normalized ratios of REE toward the MREE series, involving relatively high La_N/Sm_N ratios (up to 3.32) and Gd_N/Lu_N ratios as low as 0.45, thus tracing the MREE depletion.

When normalized against the NASC, which represents average upper continental crust exposed to weathering, the REE spider diagrams display consistently similar results (Fig. 8). The kaolinitic regolith showed a relatively flat REE pattern, with slightly more depletion in MREE than in LREE and HREE. In contrast to the parent rock and the incipiently weathered rock, the kaolin samples are depleted in REE, and their NASC-normalized REE distributions differ remarkably to that of its source rock.

The development of MREE-depleted patterns is often interpreted as being the result of acid leaching or dissolution of MREE-bearing minerals and/or amorphous mineral surface coatings (Johannesson and Zhou, 1999; Cao et al., 2001; Fernández-Caliani et al., 2009). It is reasonable to expect that feldspars breakdown was the major source of Eu leached out of the paleoweathering profile, while the loss of MREE could be due to reductive dissolution involving iron oxyhydroxide phases and concomitant release of adsorbed MREE, as noted previously. This claim is supported by the occurrence of redoximorphic features in the mottled clay horizon, such as bleached iron-free domains that have been subjected to seasonal water saturation. The preferential removal of MREE by percolating rainwater, probably in the form of stable aqueous complexes or suspended colloidal phases, is consistent with the counterpart MREE enrichment patterns reported for acid waters of the regional hydrological system (Fernández-Caliani et al., 2009), and it reflect to some extent the source-related REE signal of the water-rock interaction during regolith formation.

4.4 Stable isotope signature

Kaolinite showed $\delta^{18}O$ values ranging from 17.3‰ to 20.0‰ and averaging 19.2±1.1‰, while the δD values varied between -71‰ and -60‰ with a mean value of -65±5‰ (Table 2). The median values were as follows: 19.6‰ for $\delta^{18}O$ and -65% for δD. The isotope ratios match those reported for western European kaolins of weathering origin that formed at paleolatitudes of 35° to 40° N (compiled by Gilg et al., 2013). The intraprofile variation in the isotopic composition of kaolinite could be attributed to seasonal or annual changes in temperature and isotopic composition of infiltrating rainfall.

When plotted on a δD-$\delta^{18}O$ diagram (Fig. 9), all the values lie to the right of the supergene-hypogene line (SHL) of Sheppard et al. (1969), i.e. within the supergene field, indicating that kaolinite formed in oxygen and hydrogen isotopic equilibrium with meteoric waters at Earth-surface temperatures, as expected. It is found indeed that the data fall on or slightly to the left of the kaolinite weathering line (KWL), calculated at 20°C by using the fractionation factors of Sheppard and Gilg (1996).

4.4.1 Temperature and isotopic composition of the ancient meteoric water

At surficial temperatures, the stable isotope composition of kaolinite is related to its temperature of formation and the isotopic composition of the water from which it crystallized (e.g. Savin and Epstein, 1970; Lawrence and Taylor, 1972; Bird and Chivas, 1988; Sheppard and Gilg, 1996). Assuming that the global meteoric water line (GMWL) equation by Craig (1961) is a reasonable representation of the ancient meteoric water, which derived from the atmosphere as paleoprecipitation and percolated through the soil profile (e.g. Yapp, 2000, Delgado and Reyes, 1996; Savin and Hsieh, 1998; Tabor and Montañez, 2005; Sheldon and Tabor, 2009), the crystallization temperature of kaolinite can be estimated from the following equations:

[1] The meteoric-water equation: $\delta D_w = 8\delta^{18}O_w + 10$ (Craig, 1961)

[2] The equilibrium hydrogen isotope fractionation factor (α) between kaolinite (k) and water (w) (Gilg and Sheppard, 1996): $\delta D_k - \delta D_w = -2.2 \times 10^6\ T^{-2} - 7.7$

[3] The equilibrium oxygen isotope fractionation factor between kaolinite and water (Sheppard and Gilg, 1996): $\delta^{18}O_k - \delta^{18}O_w = 2.76 \times 10^6\ T^{-2} - 6.75$

By combining the equations [2] and [3] for kaolinite, $\delta^{18}O_w$ and δD_w can be eliminated by using the equation [1], giving the temperature of crystallization of kaolinite (in degrees Kelvin):

[4] $$T_{(K)} = \sqrt{\frac{3.04 \times 10^6}{\delta^{18}O_k - 0.125 \times \delta D_k + 7.04}}$$

This approach can be applied to clay minerals formed in open systems with high water-rock ratios and relatively low temperatures, such as surface alterations and low-temperature hydrothermal systems (Delgado and Reyes, 1996; Fernández-Caliani et al., 2010; Rosenau et al., 2013; Clauer et al., 2015; Galán et al., 2016).

An additional assumption is that kaolinite once formed in isotopic equilibrium with meteoric waters plotting on the GMWL was not subjected to any significant isotope exchange after formation. Clay minerals are extremely resistant to post-formational isotopic exchange at near surface systems (Savin and Hsieh, 1998) so that it can be argued that kaolinite retains its original isotope signature. The paleogeographic position of the Bonares profile suggests that the area was at low altitude, close to the coast, throughout the period of regolith formation, thereby modification of the isotopic composition of meteoric water by influence of topographic and continental rain-out effects can also be considered negligible.

The crystallization temperature of kaolinite obtained by applying the equation [4] to the average of the measured <2μm kaolin separates was 24.4°C. This corresponds to 23.7°C if we consider the median value. Analytical uncertainty for $\delta^{18}O$ and δD values is ±0.1‰ and ±3‰, respectively, which corresponds to uncertainties in paleotemperature estimates of about ±3°C. The warmest temperature indicated by the $\delta^{18}O$ and δD values of kaolinite (33°C) probably reflects surface-air temperatures during warm months.

For the calculated temperatures, the values of the oxygen isotope fractionation factor between kaolinite and water ($\alpha_{k\text{-}w}$) ranged from 1.0230 to 1.0257. This implies that kaolinite formed in the presence of meteoric waters with mean $\delta^{18}O$ and δD values of -5.3±0.7‰ and -32.2±5.3‰, respectively (Table 2), which should closely reflect local meteoric precipitation. Seemingly, kaolinite formed from water isotopically similar or close to modern precipitation water in the southwestern of Iberia (Carreira et al., 2009).

4.4.2 Paleoclimatic inferences

The stable isotope composition of kaolinite should reflect the paleoclimatic conditions that prevailed in the western Guadalquivir Basin during the late Neogene. The mean crystallization temperature indicated by the $\delta^{18}O$ and δD values of kaolinite (~24ºC) is higher than the present-day annual mean air temperature (~18ºC) in the study area. Subsurface temperatures tend to be approximately equal or slightly higher (+1 to 2°C) than the ambient air temperature in most climates under most soil conditions (e.g. Cerling and Quade, 1993; Sheldon and Tabor, 2009). If it is correct, the average climatic temperature of the ancient weathering system was at about 22ºC, i.e. 3-4°C warmer that today. Because the area has not been submitted to any significant change in latitude or altitude over the past five million years, the average temperature is not expected to have varied much in the past other than in response to climate warming. The combination of temperature and meteoric water isotopic values is consistent, therefore, with relatively intense kaolinitic weathering at mid-paleolatitudes.

The paleoclimate of the middle Pliocene (*ca.* 3 million years) was generally warmer and wetter than present, particularly at middle to high latitudes of Europe (Haywood et al., 2000; Salzmann et al., 2009). The ambient temperature inferred from the stable isotope record of kaolinite is in good agreement with published Pliocene mean annual temperatures (Dowsset et al., 1992; Haywood et al., 2000, Klotz et al., 2006; Pagani et al., 2009), and it may be associated with proxy estimates of high concentration of atmospheric CO_2. In fact, during the Pliocene the CO_2 levels at peak temperatures were as high as 415 ppm (Pagani et al., 2009), which have probably intensified chemical weathering and laterite formation during the warmer climate conditions.

Although a relatively warm and seasonally humid climate certainly was favorable for laterite development, the results further suggest that the combination of susceptible lithology with high rates of infiltration, efficient leaching of soluble cations and good drainage were of prime importance to kaolinite formation.

5. Conclusions

An integrated geochemical study on REE fractionation patterns and stable isotope ratios preserved in the lateritic profile of Bonares has provided new and valuable insights into soil development and climatic conditions prevailed in the southwestern margin of Iberia during the late Neogene. The resulting data have provided constraints on the past environmental conditions by providing the first estimates of paleotemperature and stable isotope composition of the ancient meteoric water.

The mineralogical and geochemical signatures of the kaolin are consistent with the hypothesized lateritic alteration of the underlying arkosic sand deposits. The kaolinitic regolith was formed by partial desilication (monosialitization) of the parent rock under mid-latitude climatic conditions warmer than today by several degrees, as indicated by the $\delta^{18}O$ and δD values of kaolinite. Significant amounts of rainwater charged with CO_2 were required for hydrolyzing primary silicates (notably alkali feldspars) and to leach all the mobile elements with the acidic percolating water, including the REE originally hosted by accessory phases like monazite. While the warm-humid climate was a major driving factor for progressive weathering reactions, the sandy parent material provided a highly permeable and easily leached substrate, thus enhancing the development of a ferricrete-capped lateritic profile at extratropical latitude location.

The results have demonstrated that the REE were mobilized and lost from the soil profile during chemical weathering and pedogenesis, and their fractionation patterns appear to be influenced by those processes. The overall REE depletion that records the paleoweathering profile relative to the bedrock is indicative of intense acid soil drainage, with preferential removal of MREE. It also reveals the inability of the kaolinitic sands to immobilize the released elements and the lack of geochemical barriers to buffer the soil acidity, such as carbonate horizons. The MREE-depleted signature is thought to arise from dissolution of iron oxyhydroxide phases under reductive conditions related to seasonal water table fluctuations, with the leached MREE lost to the drainage system.

Because of mid-Pliocene is the most recent period in the Earth's history to have experienced global warming, particularly at medium-high latitudes, the lateritic weathering profiles developed on late Neogene sediments of the Guadalquivir Basin could be useful as possible analogues for predicting future climatic and pedogenetic effects of increased atmospheric CO_2 concentration levels on the Earth´s critical zone.

Acknowledgments

This work has been partially supported by the Government of Andalusia (Spain) through the Research Group on Geology and Environmental Geochemistry (RNM-347). The paper benefited from valuable suggestions and comments made by two anonymous reviewers.

References

Abreu, M.M., 1990. Ferruginous pisolites from South of Portugal. Paleoenvironmental Quaternary relics. Sci. Géol. Bull. 43, 95-102.

Aja, S.U., 1998. The sorption of the rare earth element, Nd, onto kaolinite at 25º C. Clays Clay Min. 46, 103-109.

Ambrosi, J.P., Nahon, D., 1986. Petrological and geochemical differentiation of lateritic iron crust profiles. Chem. Geol. 57, 371-393.

Barron, E.J., Fawcett, P.J., Pollard, D., Thompson, S.L., 1993. Model simulations of Cretaceous climates: the role of geography and carbon dioxide. Philos. Trans. R. Soc. London, Ser. B 341, 307–376.

Bau, M., 1999. Scavenging of dissolved yttrium and rare earths by precipitating iron oxyhydroxide: experimental evidence for Ce oxidation, Y-Ho fractionation, and lanthanide tetrad effect. Geochim. Cosmochim. Acta 63, 67-77.

Bird, M.I., Chivas, A.R., 1988. Stable-isotope evidence for low-temperature kaolinitic weathering and post-formational hydrogen-isotope exchange in Permian kaolinites. Chem. Geol. 72, 249-265.

Bird, M.I, Chivas, A.R., 1989. Stable-isotope geochronology of the Australian regolith. Geochim. Cosmochim. Acta 53, 3239-3256.

Braun, J.J., Pagel, M., Herbillon, A., Rosin, C., 1993. Mobilization and redistribution of

REEs and thorium in a syenitic lateritic profile: A mass balance study. Geochim. Cosmochim. Acta 57, 4419-4434.

Cao, X., Chen, Y., Wang, X., Deng, X., 2001. Effects of redox potential and pH value on the release of rare earth elements from soil. Chemosphere, 44, 655-661.

Carreira, P.M., Nunes, D., Valerio, P., Araujo, M.F., 2009. A 15-year record of seasonal variation in the isotopic composition of precipitation water over continental Portugal. J. Radioanal. Nucl. Chem. 281, 153-156.

Cerling, T.E., Quade, J., 1993. Stable carbon and oxygen isotopes in soil carbonates, in: McKenzie, J.A., Savin, S. (Eds.), Climate Change in Continental Isotopic Records. Geophysics Monograph, Vol. 78, Am. Geophys. Union, Washington DC, pp. 217-231.

Civis, J., Sierro, F.J., González Delgado, J.A., Flores, J.A., Andrés, I., Porta, J., Valle, M., 1987. El Neógeno marino de la provincia de Huelva: antecedentes y definición de las unidades litoestratigráficas, in: Civis, J. (Ed.), Paleontología del Neógeno de Huelva. Ed. Univ. Salamanca, pp. 9-21.

Clauer, N., Fallick, A.E., Galán, E., Aparicio, P., Miras, A., Fernández-Caliani, J.C., Aubert, A., 2015. Stable isotope constraints on the origin of kaolin deposits from Variscan granitoids of Galicia (NW Spain). Chem. Geol. 417, 90-101.

Clayton, R.N., Mayeda, T.K., 1963. The use of bromine pentafluoride in the extraction of oxygen from oxides and silicates for isotopic analysis. Geochim. Cosmochim. Acta 27, 43-52.

Craig, H., 1961. Isotopic variations in meteoric waters. Science 133, 1702-1703.

Colin, F., Alarçon, C., Vieillard, P., 1993. Zircon: an immobile index in soils? Chem. Geol. 107, 273–276.

Coppin, F., Berger, G., Bauer, A., Castet, S., Loubet, M., 2002. Sorption of lanthanides on smectite and kaolinite. Chem. Geol. 182, 57-68.

Delgado, A., Reyes, E., 1996. Oxygen and hydrogen isotope compositions in clay minerals; a potential single mineral geothermometer. Geochim. Cosmochim. Acta 60, 4285-4289.

Díaz del Olmo, F., Recio, J.M., Barrera, C.B., Cámara, R., Barrera, F.B., 2010. New contributions to the geomorphologic characterization of aeolian littoral sand sheet at El Abalario-Doñana: Río Loro small-lake profile (Huelva, Spain). Geogaceta, 48, 3-6.

Dill, H.G., 2016. Kaolin: Soil, rock and ore: From the mineral to the magmatic, sedimentary and metamorphic environments. Earth-Sci. Rev. 161, 6-129.

Dixon J.B., Weed S.B., 1989. Minerals in Soil Environments, second ed. Soil Sci. Soc. Am. Book Series, 1, Madison.

Dowsett, H.J., Cronin, T.M., Poore, R.Z., Thompson, R.S., Whatley, R.C., Wood, A.M., 1992. Micropaleontological evidence for increased meridional heat transport in the North Atlantic Ocean during the Pliocene. Science 258, 1133-1135.

Feng, W., Yapp, C.J., 2009. $^{18}O/^{16}O$ and D/H ratios of pedogenic kaolinite in a North American Cenomanian laterite: Paleoclimatic implications. Geochim. Cosmochim. Acta 73, 6249-6263.

Fernández-Caliani, J.C., Barba-Brioso, C., De la Rosa, J.D., 2009. Mobility and speciation of rare earth elements in acid minesoils and geochemical implications for river waters in the southwestern Iberian margin. Geoderma 149, 393-401.

Fernández-Caliani, J.C., Cantano, M., 2010. Intensive kaolinization during a lateritic weathering event in South-West Spain. Mineralogical and geochemical inferences from a relict paleosol. Catena 80, 23-33.

Fernández-Caliani, J.C., Galán, E., Aparicio, P., Miras, A., Márquez, M.G., 2010. Origin and geochemical evolution of the Nuevo Montecastelo kaolin deposit (Galicia, NW Spain). Appl. Clay Sci. 49, 91-97.

Galán E., Aparicio, P., Fernández-Caliani, J.C., Miras, A., Márquez, M.G., Fallick, A.E., Clauer, N., 2016. New insights on mineralogy and genesis of kaolin deposits: The Burela kaolin deposit (Northwestern Spain). Appl. Clay Sci. 131, 14-26.

Galán, E., Fernández-Caliani, J.C., Miras, A., Aparicio, P., Márquez, M.G., 2007. Residence and fractionation of rare-earth elements during kaolinization of alkaline peraluminous granites in NW Spain. Clay Min. 42, 341-353.

Galán, E., Ferrell, R.E., 2013. Genesis of clays, in: Bergaya, F., Lagaly, G. (Eds.), Handbook of Clay Science. Developments in Clay Science, Vol. 5, Elsevier, pp. 83-126.

Galán E., Gómez-Ariza, J.L., González, I., Fernández-Caliani, J.C., Morales, E., Giráldez. I., 2003. Heavy metal partitioning in river sediments severely polluted by acid mine drainage in the Iberian Pyrite Belt. Appl. Geochem. 18, 409-421.

Gilg H.A., Hall A.M., Ebert K., Fallick A.E., 2013. Cool kaolins in Finland. Paleogeogr. Paleoclimatol. Paleoecol. 392, 454-462.

Gilg, H.A., Sheppard, S.M.F., 1996. Hydrogen isotope fractionation between kaolinite and water revisited. Geochim. Cosmochim. Acta 60, 529-533.

Girard, J.P., Freyssinet, P., Chazot, G., 2000. Unraveling climatic changes from intraprofile variation in oxygen and hydrogen isotopic composition of goethite and kaolinite in laterites: An integrated study from Yaou, French Guiana. Geochim. Cosmochim. Acta 64, 409-426.

Gómez-Ortiz, D., Fernández-Remolar, D.C., Granda, A., Quesada, C., Granda, T., Prieto-Ballesteros, O., Molina, A., Amils, R., 2014. Identification of the subsurface sulfide bodies responsible for acidity in Río Tinto source water, Spain. Earth Planet. Sci. Lett. 391, 36-41.

Gromet, L.P., Dymek, R.F., Haskin, L.A., Korotev, R.L., 1994. The "North American shale composite": Its compilation, major and trace element characteristics. Geochim. Cosmochim. Acta 48, 2469-2482.

Hall, A.M., Gilg, H.A., Fallick, A.E., Merritt, J.W., 2015. Kaolins in gravels and saprolites in north-east Scotland: Evidence from stable H and O isotopes for Palaeocene-Miocene deep weathering. Paleogeogr. Paleoclimatol. Paleoecol. 424, 6-16.

Haywood, A.M., Sellwood, B.W., Valdes, P.J., 2000. Regional warming: Pliocene (3 Ma) paleoclimate of Europe and the Mediterranean. Geology, 28, 1063-1066.

Jin, L., Ma, L., Dere, A., White, T., Mathur, R., Brantley, S.L., 2017. REE mobility and fractionation during shale weathering along a climate gradient. Chem. Geol. 466, 352-379.

Johannesson, K.H., Zhou, X., 1999. Origin of middle rare earth elements in acid waters of a Canadian High Arctic lake. Geochim. Cosmochim. Acta 63, 153-165.

Klotz, S., Fauquette, S., Combourieu-Nebout, N., Uhl, D., Suc, J.P., Mosbrugger, V., 2006. Seasonality intensification and long-term winter cooling as a part of the Late Pliocene climate development. Earth Planet. Sci. Lett. 241, 174-187.

Krause, J.M., Bellosi, E.S., Raigemborn, M.S., 2010. Lateritized tephric palaeosols from Central Patagonia, Argentina: A southern high-latitude archive of Palaeogene global greenhouse conditions. Sedimentology 57, 1721-1749.

Larrasoaña, J.C., Civis, J., Abad, M., Ledesma, S., Mata, M.P., Mediavilla, C., Ortiz, J.E., Pérez-Asensio, J.N., Ruiz, F., Salazar, A., Salvany, J.M., Sierro, F.J., Torres, T., Van den Berg, B.C.J., 2013. Chronostratigraphy of the Lower Guadalquivir Basin: an update and future challenges. V RCANS Congress Abstract Book, Huelva, Spain, p. 18-19.

Laveuf, C., Cornu, S., 2009. A review on the potentially of Rare Earth Elements to trace pedogenetic processes. Geoderma, 154, 1-12.

Laveuf, C., Cornu, S., Guilherme, L.R.G., Guerin, A., Juillot, F., 2012. The impact of redox conditions on the rare earth element signature of redoximorphic features in a soil sequence developed from limestone.

Laveuf, C., Cornu, S., Juillot, F., 2008. Rare earth elements as tracers of pedogenetic processes. C.R. Geoscience, 340, 523-532.

Lawrence, J.R., Taylor, H.P. (1972). Hydrogen and oxygen isotope systematics in weathering profiles. Geochim. Cosmochim. Acta 36, 1377-1393.

Ma, L., Jin, L., Brantley, S.L., 2011. How mineralogy and slope aspect affect REE release and fractionation during shale weathering in the Susquehanna/Shale Hills critical zone observatory. Chem. Geol. 290, 31–49.

Marker A., Oliveira J.J., 1994. Climatic and morphological control of rare earth element distribution in weathering mantles on alkaline rocks. Catena 21, 179-193.

Marques, M.M., Furtado, A.F.A.S., Cardoso, J.L., 1980-81. Testemunhos de couraças ferruginosas Quaternárias no Sudoeste de Portugal (nota preliminar). Bol. Soc. Geol. Port. 22, 417-420.

Mayoral, E., Pendón, J.G., 1986-87. Icnofacies y sedimentación en zona costera. Plioceno superior (?), litoral de Huelva. Acta Geol. Hisp. 21-22, 507-513.

Minařík, L., Žigová, A., Bendl, J., Skřivan, P., Šťastný, M., 1998. The behaviour of rare-earth elements and Y during the rock weathering and soil formation in the Ricany granite massif, Central Bohemia. Sci. Total Env. 215, 101-111.

Moore, C.L., 1996. Evaluation of regolith development and element mobility during weathering using the isocon technique. Geol. Soc. Australia Spec. Publ. 20, 141-147.

Moore, D.M., Reynolds R.C., 1997. X-Ray Diffraction and the Identification and Analysis of Clay Mineral, second ed. Oxford Univ. Press, 378 pp.

Nesbitt, H.W., 1979. Mobility and fractionation of rare earth elements during weathering of a granodiorite. Nature 279, 206–210.

Nesbitt, H.W., Young, G.M., 1982. Early Proterozoic climates and past plate motions inferred from major element chemistry of lutites. Nature 299, 715–717.

Núñez, M.A., Recio, J.M., 2007. Kaolinitic paleosols in the south west of the Iberian Peninsula (Sierra Morena region, Spain). Paleoenvironmental implications. Catena 70, 388-395.

Öhlander, B., Land, M., Ingri, J., Widerlund, A., 1996. Mobility of rare earth elements during weathering of till in northern Sweden. Appl. Geochem. 11, 93-99.

Pagani, M., Liu, Z., LaRiviere, J., Ravelo, A.C., 2009. High Earth-system climate sensitivity determined from Pliocene carbon dioxide concentrations. Nature Geosci. 3, 27-30.

Rodríguez-Vidal, J., Mayoral, E., Pendón, J.G., 1985. Aportaciones paleoambientales al tránsito Plio-Pleistoceno en el litoral de Huelva. Actas I Reun. Cuatern. Ibér. 1, 447-459.

Rosenau N.A., Tabor, N.J., 2013. Oxygen and hydrogen isotope compositions of paleosol phyllosilicates: Differential burial histories and determination of Middle–Late Pennsylvanian low-latitude terrestrial paleotemperatures. Paleogeogr. Paleoclimatol. Paleoecol. 392, 382–397.

Rosenau N.A., Tabor, N.J., Elrick, S.D., Nelson, W.J., 2013. Polygenetic history of paleosols in middle–upper Pennsylvanian cyclothems of the Illinois Basin, USA: Part II. Integrating geomorphology, climate, and glacioeustasy. J. Sed. Res. 83, 637-668.

Salzmann, U., Haywood, A.M., Lunt, D.J., 2009. The past is a guide to the future? Comparing Middle Pliocene vegetation with predicted biome distributions for the twenty-first century. Phil. Trans. R. Soc. A, 367, 189-204.

Savin, S.M., Epstein, S., 1970. The oxygen and hydrogen isotope geochemistry of clay minerals. Geochim. Cosmochim. Acta, 34, 25-42.

Savin, S.M., Hsieh, J.C.C., 1998. The hydrogen and oxygen isotope geochemistry of pedogenic clay minerals: principles and theoretical background. Geoderma 82, 227–253.

Schaefer, C.E.G.R., Fabris, J.D., Ker, J.C., 2008. Minerals in the clay fraction of Brazilian Latosols (Oxisols): a review. Clay Min. 43, 137-154.

Sheldon, N.D., Tabor, N.J., 2009. Quantitative paleoenvironmental and paleoclimatic reconstruction using paleosols. Earth-Sci. Rev. 95, 1-52.

Sheppard, S.M.F., Gilg, H.A., 1996. Stable isotope geochemistry of clay minerals. Clay Min. 31, 1-24.

Sheppard, S.M.F., Nielsen, R.L., Taylor, H.P., 1969. Oxygen and hydrogen isotope ratios of clay minerals from porphyry copper deposits. Econ. Geol. 64, 755-777.

Sierro, F.J., González-Delgado, J.A., Dabrio, C.J., Flores, J.A., Civis, J., 1996. Late Neogene depositional sequences in the foreland basin of Guadalquivir (SW Spain), in: Friend, P.F., Dabrio, C.J. (Eds.), Tertiary Basins of Spain. Cambridge Univ. Press, pp. 339-345.

Tabor, N.J., Montañez, I.P., 2005. Oxygen and hydrogen isotope compositions of pedogenic phyllosilicates: development of modern surface domain arrays and implications for paleotemperature reconstructions. Palaeogeogr. Palaeoclimatol. Palaeoecol. 223, 127-146.

Tardy, Y., Roquin, C., 1992. Geochemistry and evolution of lateritic landscapes, in: Martini, I.P., Chesworth, W. (Eds.), Weathering, Soils and Paleosols. Elsevier, Amsterdam, pp. 407-443.

Taunton, A.E., Welch, S.A., Banfield, J.F., 2000. Microbial controls on phosphate and lanthanide distributions during granite weathering and soil formation. Chem. Geol. 169, 371-382.

Taylor, S.R., McLennan, S.M., 1985. The Continental Crust: Its Composition and Evolution. Blackwell Scientific, Boston.

Thiry, M., 2000. Palaeoclimatic interpretation of clay minerals in marine deposits. An outlook from the continental origin. Earth-Sci. Rev. 49, 201-221.

Thiry, M., Schmitt, J.M., Simon-Coinçon, R., 1999. Problems, progress and future research concerning paleoweathering and paleosurfaces, in: Thiry, M., Simon-Coinçon, R. (Eds.), Palaeoweathering, Palaeosurfaces and Related Continental Deposits. Spec. Publ. Int. Ass. Sediment. 27, 3-17.

Velde, B.B., Meunier, A., 2008. The Origin of Clay Minerals in Soils and Weathered Rocks. Springer, Berlin.

Vermeire, M.L., Cornu, S., Fekiacova, Z., Detienne, M., Delvaux, B., Cornélis, J.T., 2016. Rare earth elements dynamics along pedogenesis in a chronosequence of podzolic soils. Chem. Geol. 446, 163-174.

Wan, Y., Liu, C., 2005. Study on adsorption of rare earth elements by kaolinite. J. Rare Earths 23, 377-381.

Welch, S.A., Christy, A.G., Isaacson, L., Kirste, D., 2009. Mineralogical control of rare earth elements in acid sulfate soils. Geochim. Cosmochim. Acta 73, 44-64.

Yapp, C.J., 2000. Climatic implications of surface domains in arrays of δD and δ^{18}O from hydroxyl minerals: geothite as an example. Geochim. Cosmochim. Acta 64, 2009-2025.

Yusoff, Z.M., Ngwenya, B.T., Parsons, I., 2013. Mobility and fractionation of REEs during deep weathering of geochemically contrasting granites in a tropical setting, Malaysia. Chem. Geol. 349-350, 71-86.

FIGURE AND TABLE CAPTIONS

Figure 1. Simplified geological map of the study area, sketch of the lateritic profile and sample locations.

Figure 2. Vertical distribution of major minerals, chemical index of alteration (CIA) and kaolinite crystallinity index (KCI) in the paleosol profile. The CIA and KCI are derived from previous data published by Fernández-Caliani and Cantano (2010).

Figure 3. Typical particle-size distribution curve of the kaolin and SEM image of kaolinite showing aggregates of booklet-like stacked platelets.

Figure 4. Secondary electron (left) and back-scattered electron (right) SEM images, EDS spectrum and quantitative chemical analysis of a large crystal of monazite from the incipiently kaolinized parent rock.

Figure 5. Quantitative assessment of the REE losses relative to parent rock in the profile zones of the sampling section 3. Calculations have been made using Ti (data from Fernández-Caliani and Cantano, 2010) as a conservative element, following the Nesbitt's (1979) approach.

Figure 6. Isocon diagram showing average contents of REE in the kaolinized material *vs*. the REE concentrations in the parent rock. All the REE fall below the isocon line defined by relatively immobile major elements thus indicating depletion (Al, Fe and Ti mean concentrations in weight percent are from Fernández-Caliani and Cantano, 2010).

Figure 7. Comparative spider diagrams depicting parent rock-normalized (left) and NASC-normalized (right) REE concentrations in the sampling sections of the paleosol profile.

Figure 8. Plot of δD *vs*. $\delta^{18}O$ values for the <2μm kaolinite separates (red circles). The meteoric water line (Craig, 1961), the kaolinite weathering line calculated at 20°C (Sheppard and Gilg, 1996), the supergene-hypogene line (Sheppard et al., 1969) and the isotopic composition of modern ocean water (SMOW) are given for reference. The dashed tie-line connects the mean isotope composition of the meteoric water from which kaolinite formed in equilibrium at about 24°C. Abundances are expressed as parts per thousand relative to Vienna Standard Mean Ocean Water (VSMOW).

Table 1. Concentrations of REE (mg kg^{-1}) in the studied samples and ratios of normalized values.

Table 2. Results of the stable isotope analysis. Oxygen ($\delta^{18}O_k$) and hydrogen (δD_k) isotope ratios of kaolinite (k), temperature of crystallization (T), isotope fractionation (1000 ln α), and oxygen ($\delta^{18}O_w$) and hydrogen (δD_w) isotope ratios of meteoric water (w) from which kaolinite formed in equilibrium.

Table 1

REE (mg kg^{-1})	La	Ce	Pr	Nd	Sm	Eu	Gd	Tb	Dy	Ho	Er	Tm	Yb	Lu	ΣREE	Eu/Eu*	La_N/Lu_N	La_N/Sm_N	Gd_N/Lu_N
Detection Limit	0.1	0.1	0.05	0.1	0.1	0.05	0.1	0.1	0.1	0.1	0.1	0.05	0.1	0.04	-	-	-	-	-
Section 1																			
CH-5	18.6	37.2	4.43	15.2	3.1	0.56	2.7	0.5	3.1	0.6	2.0	0.31	2.1	0.32	90.72	0.83	0.97	1.53	0.57
CH-4a	28.9	51.5	5.53	16.7	2.8	0.60	2.4	0.4	3.0	0.7	2.1	0.32	2.2	0.35	117.50	0.99	1.37	2.64	0.46
CH-4b	25.5	42.6	4.51	13.9	2.4	0.51	2.0	0.4	2.6	0.6	1.7	0.28	1.9	0.29	99.19	0.99	1.46	2.72	0.47
CH-3	10.1	17.0	1.83	5.6	1.0	0.19	0.8	0.2	1.0	0.2	0.7	0.12	0.8	0.12	39.66	0.91	1.40	2.58	0.45
CH-2	15.2	27.5	2.68	7.6	1.3	0.23	1.0	0.2	1.0	0.2	0.6	0.09	0.6	0.09	58.29	0.86	2.81	2.99	0.75
CH-1	13.9	30.1	3.37	11.4	2.2	0.40	1.5	0.2	1.3	0.3	0.8	0.12	0.8	0.12	66.51	0.94	1.92	1.61	0.84
Section 2																			
PTB-4	22.1	32.8	3.70	9.2	1.7	0.34	1.4	0.2	1.5	0.3	1.0	0.16	1.0	0.17	75.57	0.94	2.16	3.32	0.56
PTB-3	12.0	22.8	2.6	8.0	1.4	0.25	0.9	0.1	0.8	0.2	0.5	0.08	0.5	0.08	50.21	0.95	2.49	2.19	0.76
PTB-2	10.8	23.5	3.51	13.3	3.1	0.73	2.0	0.3	1.5	0.3	0.7	0.11	0.7	0.10	60.65	1.25	1.79	0.89	1.35
PTB-1	31.3	59.2	8.96	34.2	8.0	1.84	7.7	1.2	6.9	1.4	3.8	0.54	3.4	0.52	168.96	1.00	1.00	1.00	1.00
Section 3																			
BO-8	7.1	10.5	1.28	4.2	0.9	0.15	0.7	0.1	0.8	0.2	0.5	0.08	0.6	0.08	27.19	0.84	1.47	2.02	0.59
BO-5	24.3	40.0	4.43	13.2	2.4	0.49	1.8	0.3	2.0	0.4	1.2	0.19	1.3	0.20	92.21	1.05	2.02	2.59	0.61
BO-4	14.6	24.5	2.50	7.2	1.3	0.24	1.1	0.2	1.3	0.3	0.8	0.14	0.9	0.14	55.22	0.89	1.73	2.87	0.53
BO-3	8.9	13.7	1.67	4.6	0.8	0.17	0.6	0.1	0.7	0.1	0.4	0.07	0.5	0.07	32.38	1.09	2.11	2.84	0.58
BO-2	9.9	16.4	2.06	6.6	1.3	0.24	1.0	0.2	0.9	0.2	0.6	0.09	0.6	0.10	40.19	0.93	1.64	1.95	0.68
BO-1	11.8	26.0	3.67	13.7	3.0	0.71	2.0	0.3	1.5	0.3	0.7	0.11	0.7	0.10	64.59	1.29	1.96	1.01	1.35
BO-0	32.6	89.0	10.7	39.6	9.3	1.85	6.5	0.9	4.9	0.9	2.6	0.39	2.7	0.41	202.35	1.06	1.32	0.90	1.07

ΣREE= Total REE; Eu/Eu*= Eu_N / (Sm_N x Gd_N)$^{0.5}$. The subscript N denotes normalized values.

Table 2

Sample	**$\delta^{18}O_k$**	**δD_k**	**T (°C)**	**1000 ln α**	**α_{k-w}**	**$\delta^{18}O_w$**	**δD_w**
PTB-2	20.0	-60	24	24.5	1.0248	-4.5	-26.0
CH-2	19.8	-60	25	24.3	1.0246	-4.5	-26.0
BO-2A	17.3	-65	33	22.7	1.0230	-5.4	-33.2
BO-2B	19.4	-71	20	25.4	1.0257	-6.0	-38.0
CH-1	19.6	-69	21	25.1	1.0254	-5.5	-34.0
Average	19.2 ± 1.1	-65 ± 5.0	24.4 ± 5.1	24.5 ± 1.0	1.0248 ± 0.001	-5.3 ± 0.7	-32.2 ± 5.3

Figure 1

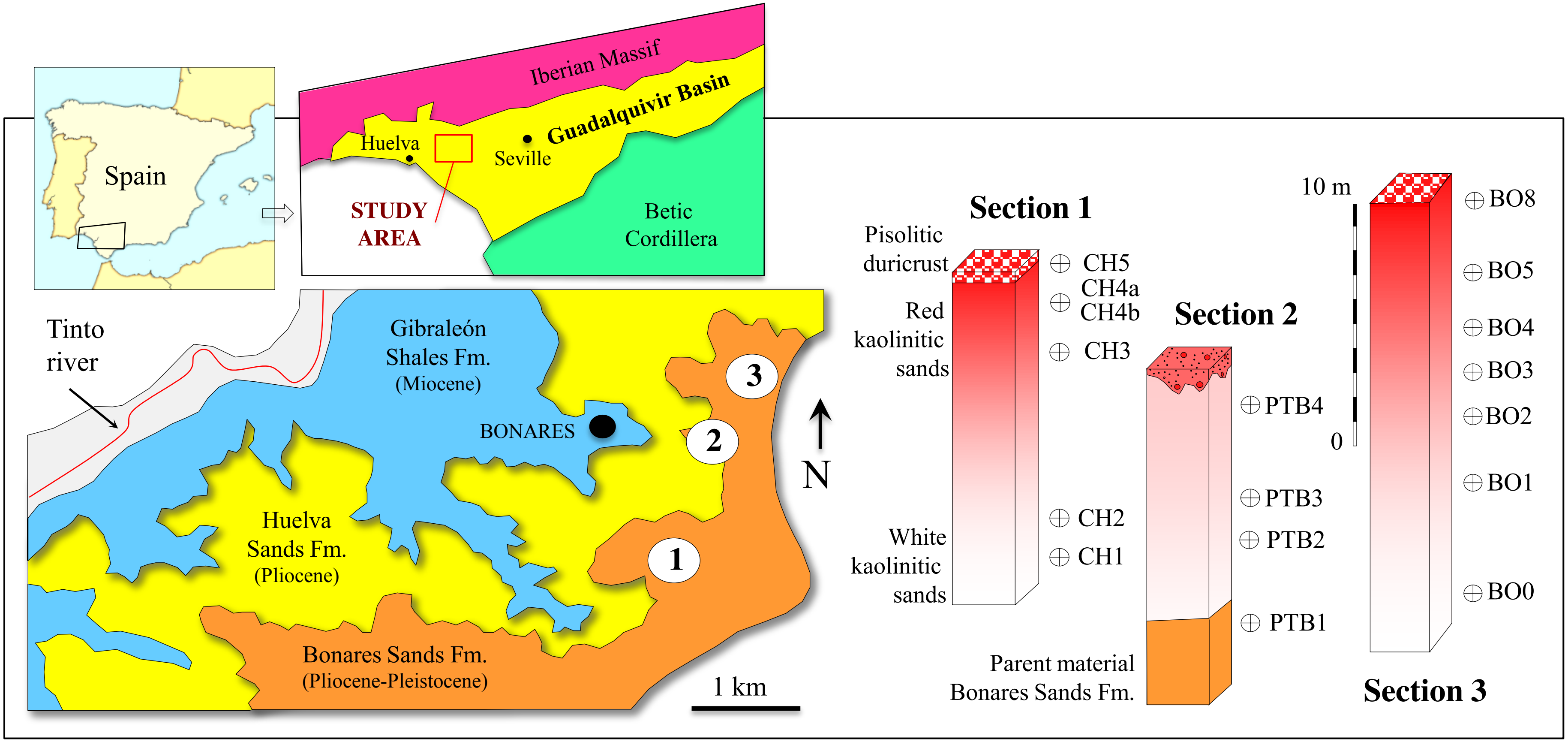
Spain
Iberian Massif
Guadalquivir Basin
Huelva
Seville
STUDY AREA
Betic Cordillera
Tinto river
Gibraleón Shales Fm. (Miocene)
BONARES
Huelva Sands Fm. (Pliocene)
Bonares Sands Fm. (Pliocene-Pleistocene)
1
2
3
N
1 km
Section 1
Pisolitic duricrust
Red kaolinitic sands
White kaolinitic sands
CH5
CH4a
CH4b
CH3
CH2
CH1
Section 2
PTB4
PTB3
PTB2
PTB1
Parent material Bonares Sands Fm.
10 m
0
Section 3
BO8
BO5
BO4
BO3
BO2
BO1
BO0

Figure 2

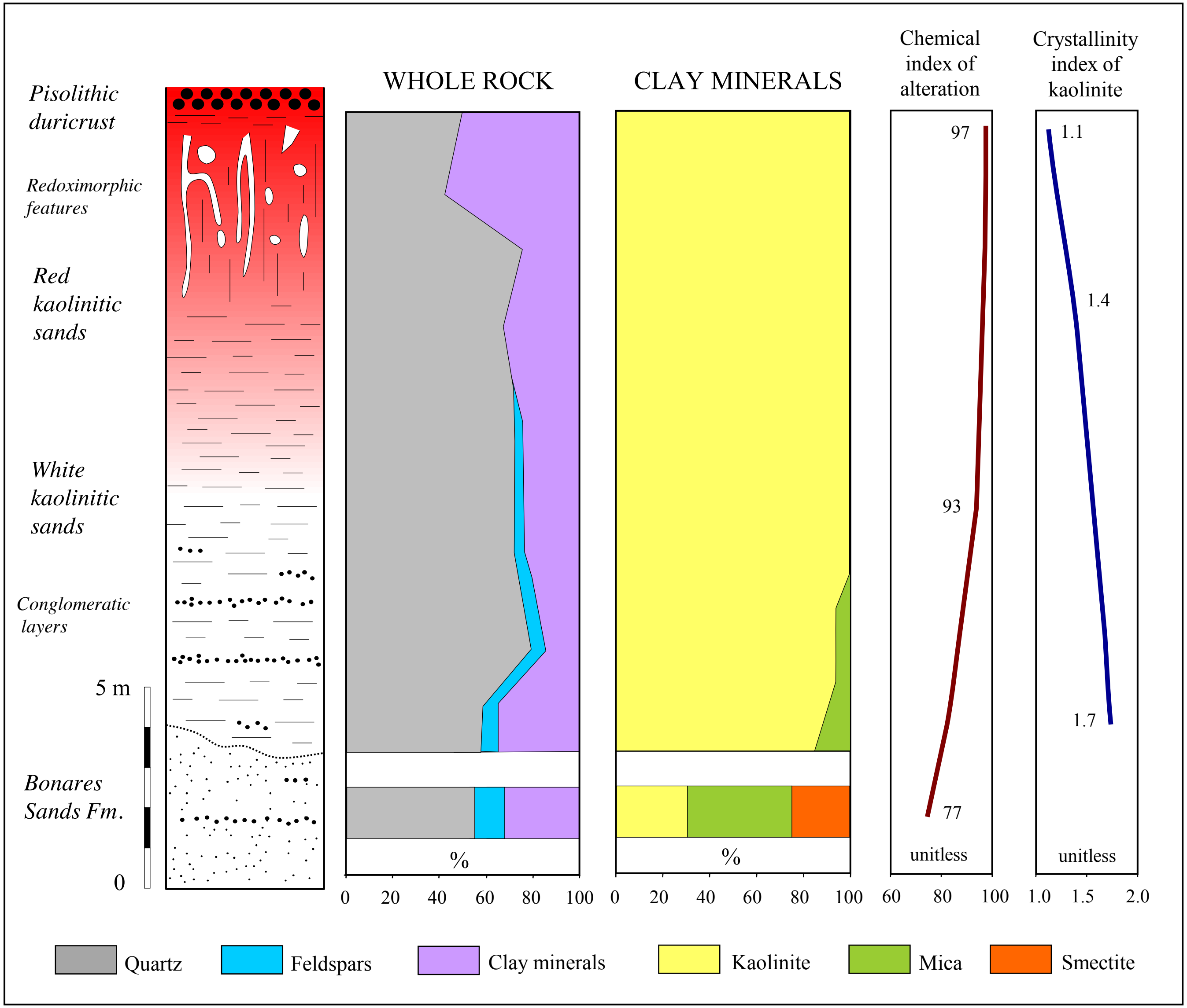

Pisolithic duricrust
Redoximorphic features
Red kaolinitic sands
White kaolinitic sands
Conglomeratic layers
5 m
Bonares Sands Fm.
0
WHOLE ROCK
%
0 20 40 60 80 100
CLAY MINERALS
%
0 20 40 60 80 100
Chemical index of alteration
97
93
77
unitless
60 80 100
Crystallinity index of kaolinite
1.1
1.4
1.7
unitless
1.0 1.5 2.0
Quartz
Feldspars
Clay minerals
Kaolinite
Mica
Smectite

Figure 3

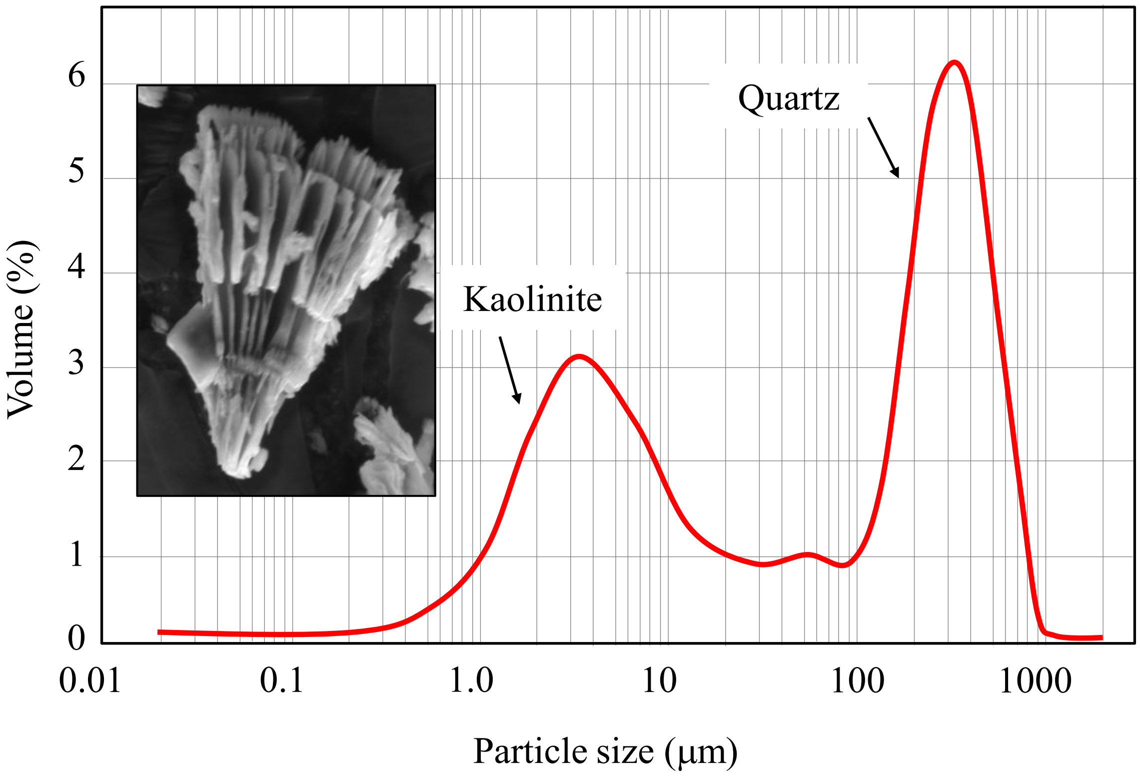
Volume (%)
0
1
2
3
4
5
6
Quartz
Kaolinite
0.01
0.1
1.0
10
100
1000
Particle size (µm)

Figure 4

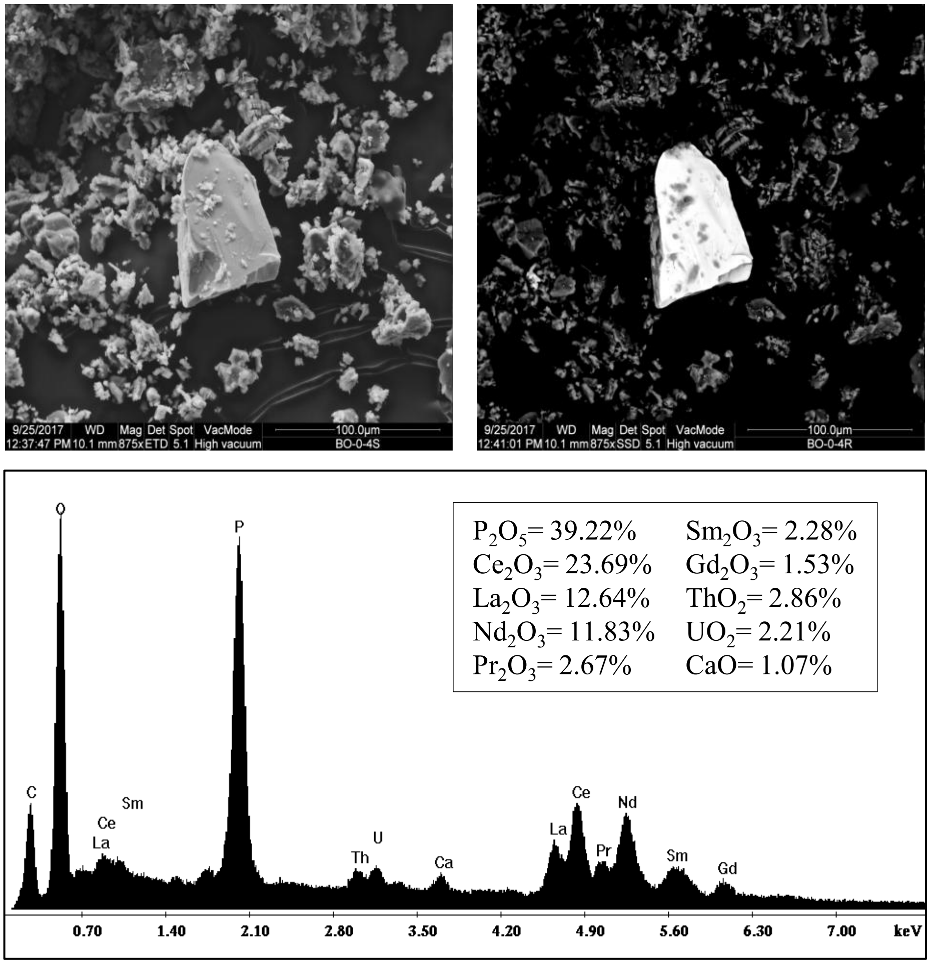
9/25/2017 WD Mag Det Spot VacMode 100.0µm
12:37:47 PM 10.1 mm 875x ETD 5.1 High vacuum BO-0-4S
9/25/2017 WD Mag Det Spot VacMode 100.0µm
12:41:01 PM 10.1 mm 875x SSD 5.1 High vacuum BO-0-4R
P_2O_5= 39.22%
Ce_2O_3= 23.69%
La_2O_3= 12.64%
Nd_2O_3= 11.83%
Pr_2O_3= 2.67%
Sm_2O_3= 2.28%
Gd_2O_3= 1.53%
ThO_2= 2.86%
UO_2= 2.21%
CaO= 1.07%
O
P
C
Ce
La
Sm
Th
U
Ca
Ce
La
Nd
Pr
Sm
Gd
0.70
1.40
2.10
2.80
3.50
4.20
4.90
5.60
6.30
7.00
keV

Figure 5

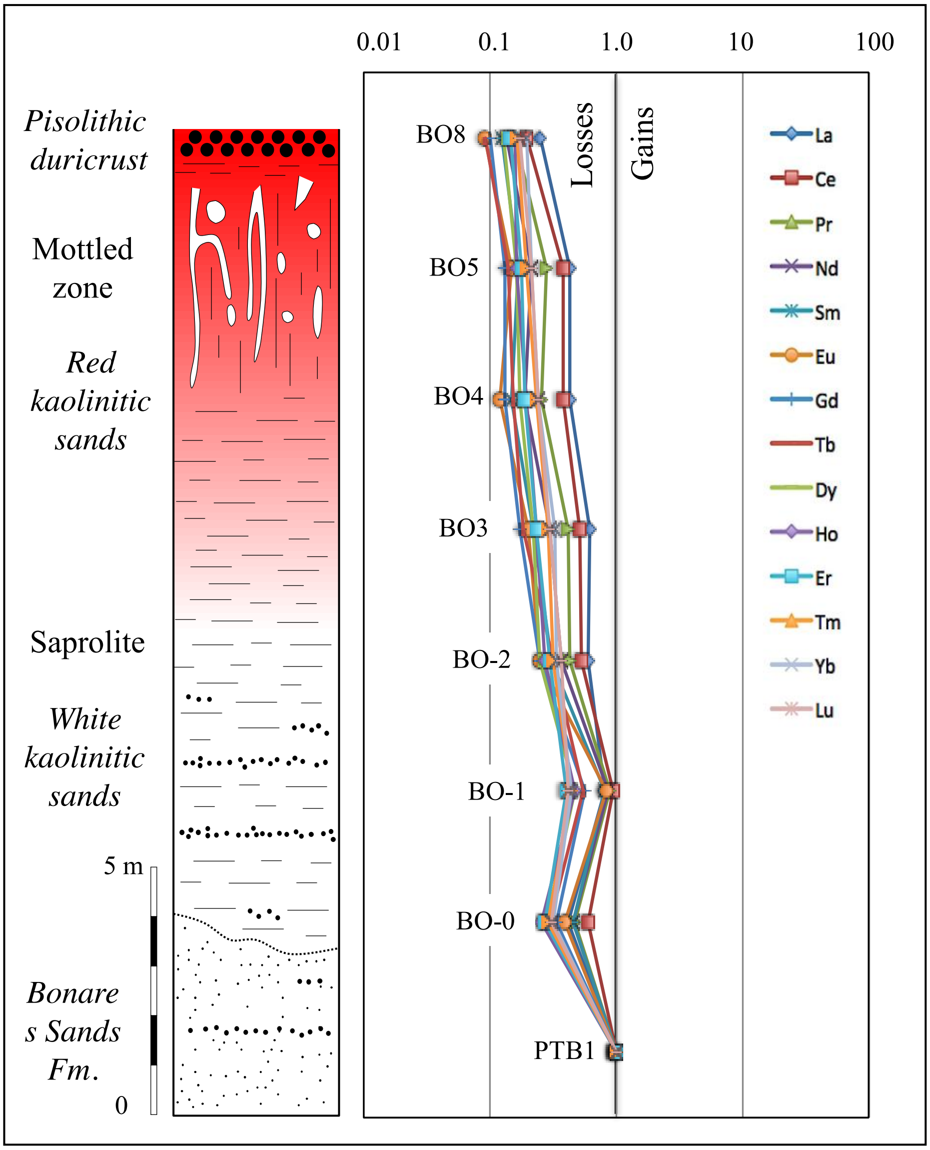
0.01
0.1
1.0
10
100
Pisolithic duricrust
Mottled zone
Red kaolinitic sands
Saprolite
White kaolinitic sands
Bonares Sands Fm.
5 m
0
BO8
BO5
BO4
BO3
BO-2
BO-1
BO-0
PTB1
Losses
Gains
La
Ce
Pr
Nd
Sm
Eu
Gd
Tb
Dy
Ho
Er
Tm
Yb
Lu

Figure 6

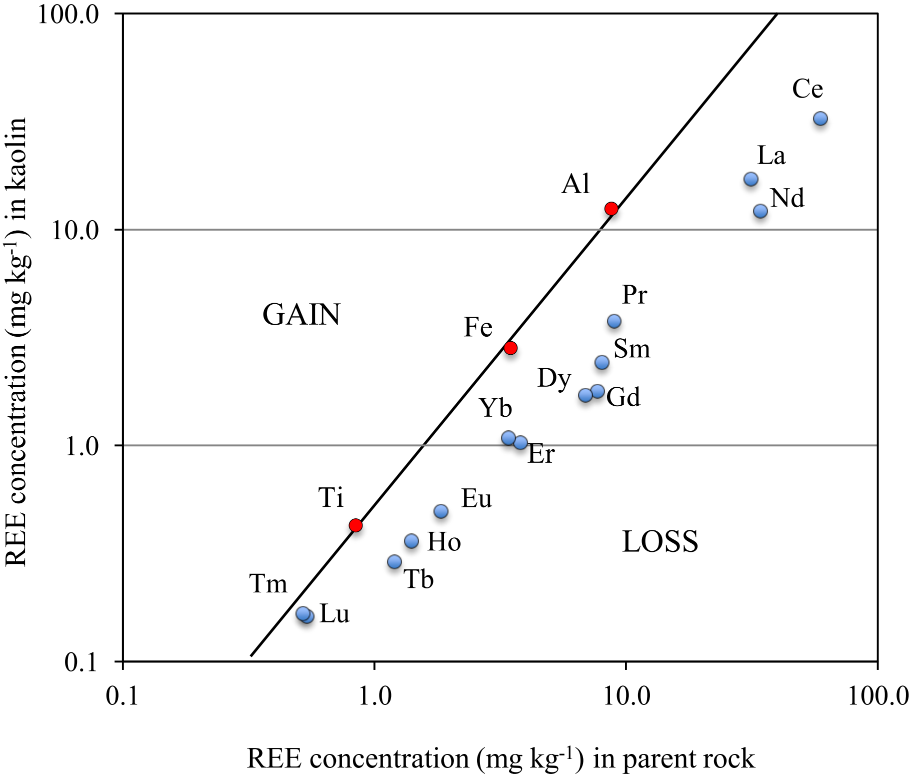
Ce
La
Al
Nd
Pr
GAIN
Fe
Sm
Dy
Gd
Yb
Er
Ti
Eu
Ho
LOSS
Tb
Tm
Lu
100.0
10.0
1.0
0.1
0.1
1.0
10.0
100.0
REE concentration (mg kg-1) in kaolin
REE concentration (mg kg-1) in parent rock

Figure 7

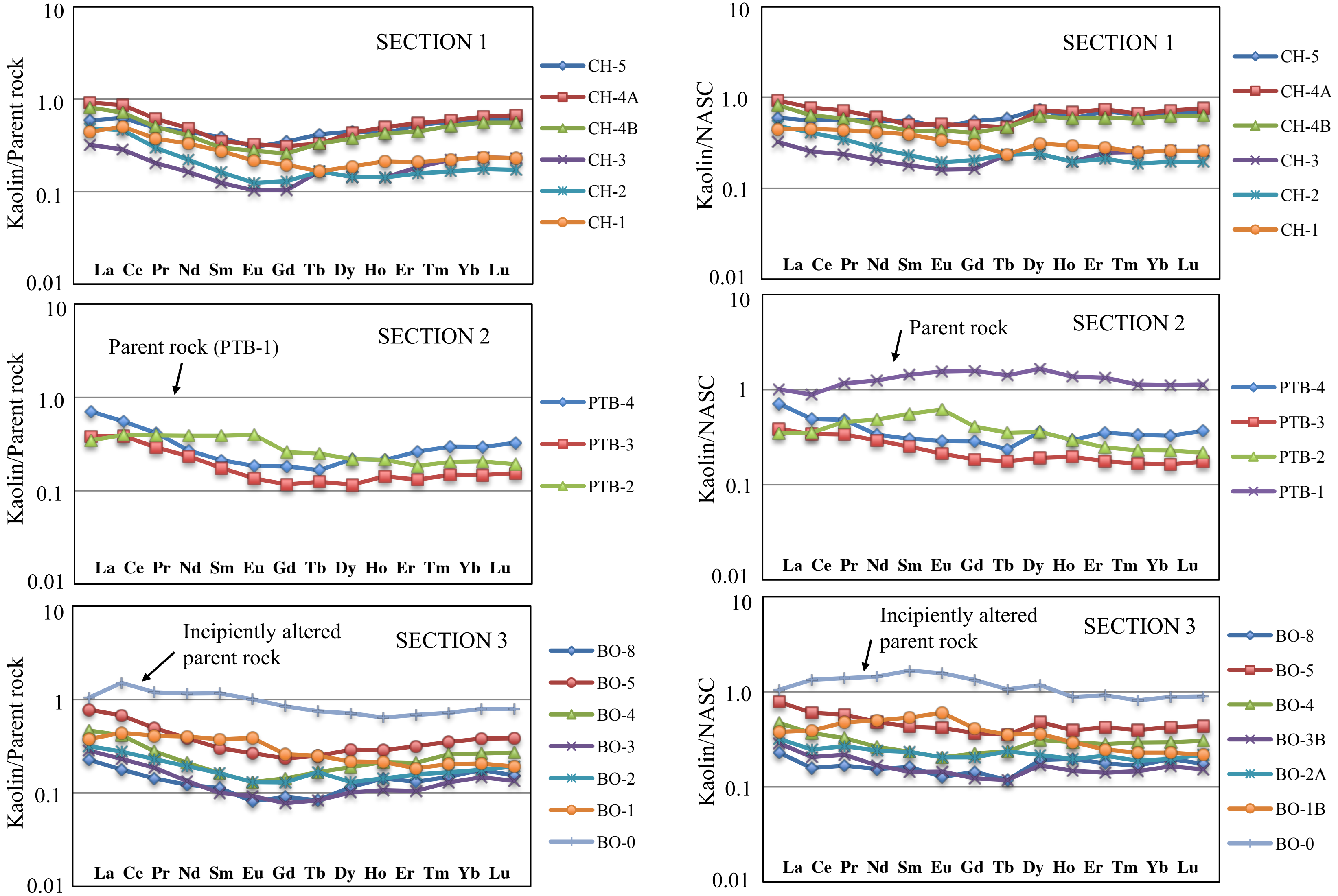
SECTION 1
Kaolin/Parent rock
10
1.0
0.1
0.01
La Ce Pr Nd Sm Eu Gd Tb Dy Ho Er Tm Yb Lu
CH-5
CH-4A
CH-4B
CH-3
CH-2
CH-1
SECTION 1
Kaolin/NASC
10
1.0
0.1
0.01
La Ce Pr Nd Sm Eu Gd Tb Dy Ho Er Tm Yb Lu
CH-5
CH-4A
CH-4B
CH-3
CH-2
CH-1
Parent rock (PTB-1)
SECTION 2
Kaolin/Parent rock
10
1.0
0.1
0.01
La Ce Pr Nd Sm Eu Gd Tb Dy Ho Er Tm Yb Lu
PTB-4
PTB-3
PTB-2
Parent rock
SECTION 2
Kaolin/NASC
10
1
0.1
0.01
La Ce Pr Nd Sm Eu Gd Tb Dy Ho Er Tm Yb Lu
PTB-4
PTB-3
PTB-2
PTB-1
Incipiently altered parent rock
SECTION 3
Kaolin/Parent rock
10
1
0.1
0.01
La Ce Pr Nd Sm Eu Gd Tb Dy Ho Er Tm Yb Lu
BO-8
BO-5
BO-4
BO-3
BO-2
BO-1
BO-0
Incipiently altered parent rock
SECTION 3
Kaolin/NASC
10
1.0
0.1
0.01
La Ce Pr Nd Sm Eu Gd Tb Dy Ho Er Tm Yb Lu
BO-8
BO-5
BO-4
BO-3B
BO-2A
BO-1B
BO-0

Figure 8

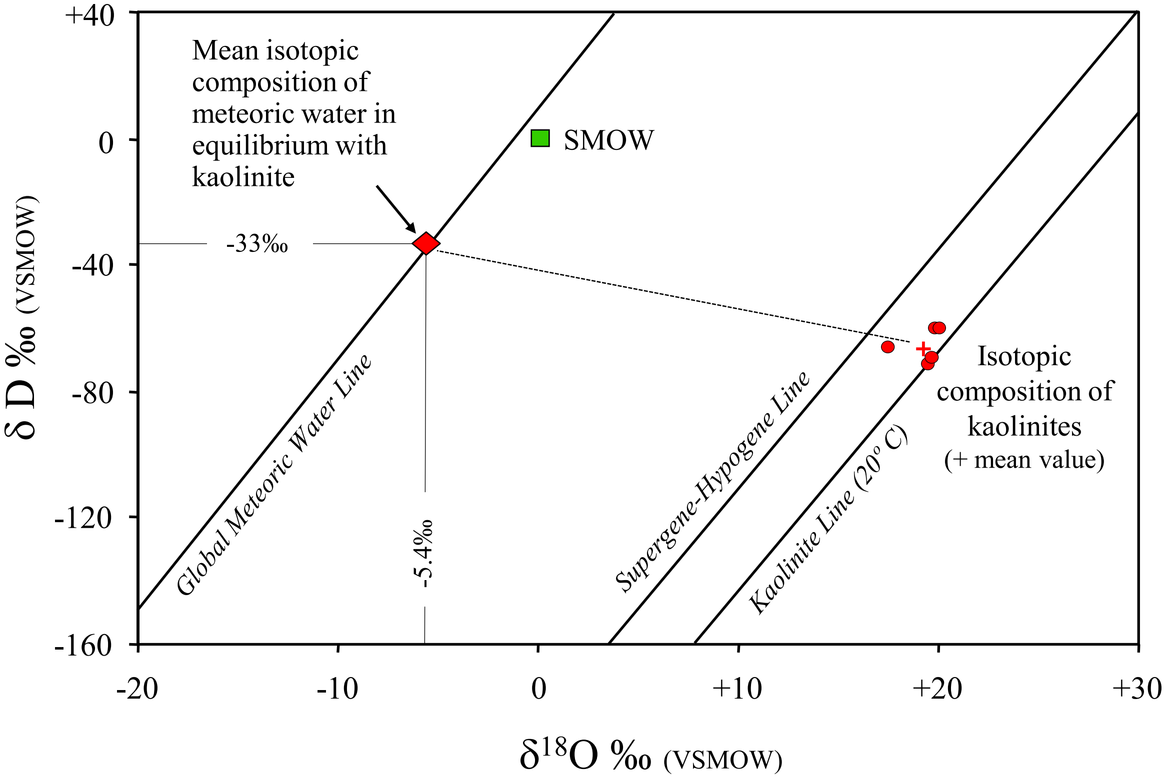

Mean isotopic composition of meteoric water in equilibrium with kaolinite
SMOW
-33‰
-5.4‰
Global Meteoric Water Line
Supergene-Hypogene Line
Kaolinite Line (20° C)
Isotopic composition of kaolinites
(+ mean value)
+40
0
-40
-80
-120
-160
-20
-10
0
+10
+20
+30
δ D ‰ (VSMOW)
δ18O ‰ (VSMOW)